Precision Plasmonics with Monomers and Dimers of Spherical Gold Nanoparticles: Nonequilibrium Dynamics at the Time and Space Limits

L. Schumacher,[†] J. Jose,[†] D. Janoschka,[‡] P. Dreher,[‡] T. J. Davis,[‡,∥] M. Ligges,[‡] R. Li,[§] M. Mo,[§] S. Park,[§] X. Shen,[§] S. Weathersby,[§] J. Yang,[§] X. Wang,[§] F. Meyer zu Heringdorf,[*,‡] K. Sokolowski-Tinten,[*,‡] and S. Schlücker[*,†]

[†]Department of Chemistry and Center for Nanointegration Duisburg-Essen (CENIDE), University of Duisburg-Essen, 45141 Essen, Germany

[‡]Department of Physics and Center for Nanointegration Duisburg-Essen (CENIDE), University of Duisburg-Essen, 47057 Duisburg, Germany

[§]SLAC National Accelerator Laboratory, Menlo Park, California 94025, United States

ABSTRACT: Monomers and dimers of spherical gold nanoparticles (NPs) exhibit highly uniform plasmonic properties at the single-particle level due to their high structural homogeneity (precision plasmonics). Recent investigations in precision plasmonics have largely focused on static properties using conventional techniques such as transmission electron microscopy and optical dark-field microscopy. In this Feature Article, we first highlight the application of femtosecond time-resolved electron diffraction for monitoring the nonequilibrium dynamics of spherical gold NPs after ultrafast optical excitation. The analysis of the transient diffraction patterns allows us to directly obtain quantitative information on the incoherent excitation of the lattice, that is, heating upon electron−lattice equilibration, as well as on the development of strain due to lattice expansion on picosecond time scales. The controlled assembly of two spherical gold NPs into a dimer with a few nanometers gap leads to unique optical properties. Specifically, extremely high electric fields (hot spot) in the gap are generated upon resonant optical excitation. Conventional optical microscopy cannot spatially resolve this unique hot spot due to the optical diffraction limit. We therefore employed nonlinear photoemission electron microscopy to visualize hot spots in single dimers of spherical gold NPs. A quantitative comparison of different single dimers confirms the homogeneity of the hot spots on the single-particle level. Overall, these initial results are highly encouraging because they pave the way to investigate nonequilibrium dynamics in highly uniform plasmonic nanostructures at the time and space limits.

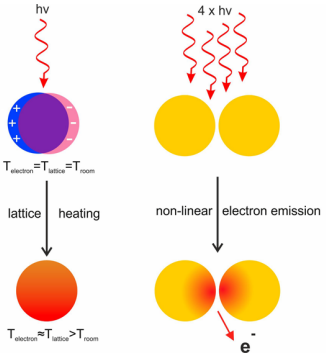

1. INTRODUCTION

Noble-metal nanoparticles (NPs) support localized surface plasmon resonances (LSPRs) upon optical excitation: When the incident optical frequency is resonant with the plasma frequency, then the oscillating electric field of the light wave drives the coherent oscillation of the free electron gas in the metal (see Figure 1). After the excitation of an LSPR, also called particle plasmon to distinguish it from propagating plasmons in an extended film, there are two distinct decay channels: a radiative pathway (scattering) and a nonradiative pathway (absorption).[1] In the radiative pathway (Figure 1, top), the metal NP acts as a nanoantenna that emits radiation as a Hertzian dipole with nanoscale dimensions. Because the frequency of the emitted photons is the same as the one of the incident photons, elastic scattering takes place, which can be measured from single particles, for example, in a dark-field microscopic configuration. In the nonradiative pathway (Figure 1 bottom), the metal NP essentially acts as an absorbing medium in which charge separation occurs and hot charge carriers (hot electrons and hot holes) are generated. After electron−electron scattering, occurring on a femtosecond time scale, the energy initially stored in the electronic system is dissipated to the lattice on picosecond time scales via electron−phonon coupling processes.[2] The plasma frequency or plasmon wavelength for which this LSPR occurs depends on parameters such as the metal/material, the size, the shape, and the surrounding medium. The latter has been extensively exploited for LSPR sensing.[3]

Also, the different decay channels of a plasmon can be exploited in various areas of physical chemistry, medicine, and material science. Surface-enhanced Raman scattering (SERS)[4] of molecules adsorbed on noble-metal NPs is a prominent representative of a whole class of surface-enhanced molecular spectroscopic techniques (Raman/IR/fluorescence). Essen-

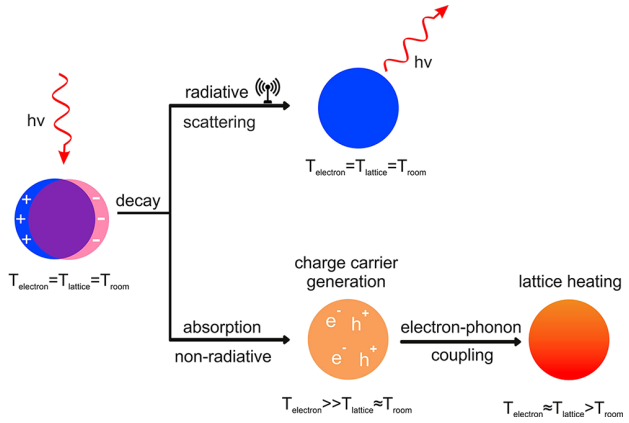

Figure 1. Photoexcitation and subsequent decay processes in a plasmonic nanoparticle following illumination with a laser pulse. The incident electric field induces the oscillation of free electron gas in the nanoparticle called plasmon resonance. This plasmon is damped radiatively by the re-emission of photons (top) and nonradiatively via hot carrier generation and subsequent lattice heating due to electron–phonon coupling (bottom). $T_{electron}$, $T_{lattice}$, and T_{room} represent the temperature corresponding to the electron system, the lattice, and the environment, respectively.

tially, the locally enhanced electric field due to LSPR excitation leads to very large induced dipoles, creating intense Raman scattering. In this sense, the metal NP acts as an optical enhancer for this type of plasmon-assisted scattering from molecules. In addition to this "passive" way of the radiative channel (scattering) employed in optical spectroscopy, the nonradiative channel (absorption) has attracted more and more attention in recent years. The localized generation and extraction of hot carriers emerges as an attractive route for applications in photovoltaics, photochemistry, and photocatalysis.[1,5−9] However, the carrier lifetime is limited by electron–phonon coupling processes, and the energy transfer to the phonon system leads to rapid heating of the lattice. Therefore, NPs are also used as nanoscale sources of thermal and mechanical energy (see the review by Baffou et al.[10] and references therein). The strength of electron–phonon coupling depends on the specific material but is also influenced by the sample morphology. In particular, on the nanoscale, size and shape as well as surface and interface effects can play an important role.[11,12] The majority of experimental work addressing electron–phonon coupling in NPs makes use of time-resolved optical techniques, for example, femtosecond transient absorption (see the review by Hartland et al.[13] and references therein). More recently, ultrafast X-ray or electron diffraction/scattering has also been applied to directly monitor various aspects of the structural response of nanostructured materials upon optical excitation.[14−31]

Here we extend our previous time-resolved diffraction studies on the electron–lattice relaxation in nanoscale Au[26,29] to the case of highly spherical NPs (AuNSs, Section 2). This allows us to directly obtain quantitative information on the incoherent excitation of the lattice (i.e., heating) upon electron–lattice equilibration as well as on the development of strain due to lattice expansion.

A single noble-metal NP may be viewed as the equivalent of a single atom in molecular chemistry. Similar to molecular chemistry, where molecules can be considered as an assembly of atoms sharing electrons by bonding molecular orbitals, assemblies of more than one metal particle exhibit new physical properties. A dimer of two metal NPs is the simplest case for which plasmonic coupling, the analogue of the linear combination of atomic orbitals (LCAO) concept in quantum chemistry, occurs. The arrows in Figure 2 indicate the generated dipole moment, that is, charge separation, upon LSPR excitation.

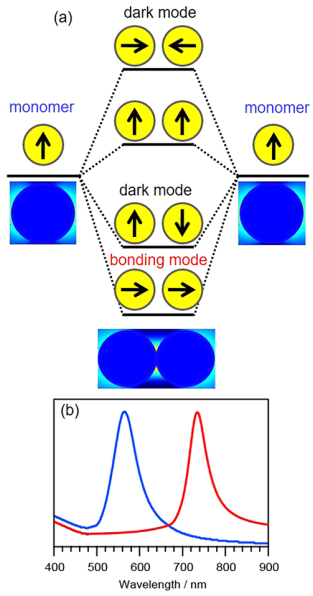

Figure 2. (a) Plasmon hybridization diagram for a dimer of spherical gold nanoparticles. Hybridization results in the formation of bonding and antibonding plasmon modes, which are lower and higher in energy, respectively, with reference to a monomer plasmon mode; arrows represent the direction of the induced dipole. Dark plasmon modes are modes with zero effective induced dipole moment, which makes them invisible in optical spectroscopy. The enhancement of the electric field in the junction between the spheres is evident from the near-field diagram. (b) The blue curve in the optical spectrum represents the LSPR coupling mode of the monomer, and the red-shifted curve represents the longitudinal bonding dipolar mode of the dimer.[32,33]

The coupling of the dipoles excited on the two spheres in a dimer can occur in the direction of the dimer axis (σ-type orbital in quantum chemistry terms) or perpendicular to it (π-type orbital in quantum chemistry terms). Overall, four new plasmon modes arise: two bonding modes with energies lower and two antibonding modes with energies higher than the energy required for the LSPR excitation in a single sphere.[32,33] In other words, a dimer of two noble-metal NPs may be considered as the colloidal equivalent of a homonuclear diatomic molecule, such as molecular hydrogen (H_2), nitrogen (N_2), oxygen (O_2), or a halogen (X_2). Only the two plasmon modes associated with a dipole moment are observable in optical spectroscopy: the longitudinal bonding dipolar plasmon (LBDP) mode with the lowest energy (highest wavelength) and the transversal antibonding dipolar plasmon mode with the highest energy (lowest wavelength).

Theory typically employs idealized structures such as perfect spheres. Experimentalists have long lagged behind in the preparation of such perfect noble-metal NPs. Only for a few years have colloid chemists been able to synthesize highly round gold NPs by etching (oxidizing) the more reactive atoms at higher-order facets, thereby paving the way to precision plasmonics, that is, high reproducibility at the single-particle

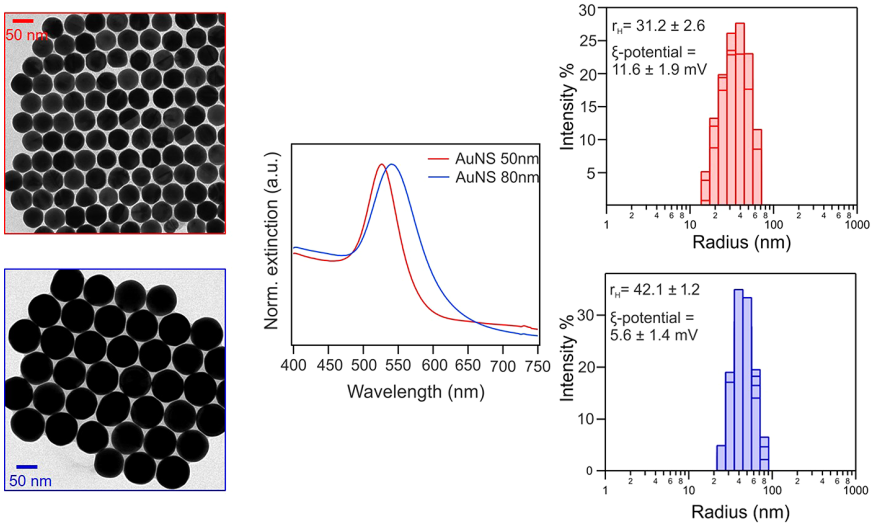

Figure 3. (left) Characterization of ideal gold spheres of varying sizes using different techniques: Transmission electron microscopy (TEM) reveals that both 50 and 80 nm spheres are highly uniform in size and structure. (middle) Extinction spectra of monomer spheres showing an increased scattering for the bigger 80 nm particles, as expected. (right) Zeta potential measurements and dynamic light scattering (DLS) showing that the particles are positively charged due to the presence of CTAB capping agent and the hydrodynamic radius, respectively.

level.[34] These highly spherical gold NPs, or gold nanospheres (AuNSs), can then be assembled into highly defined ideal dimers with gap control at the angstrom level by using molecular linkers (Section 3). Their single-particle dark-field scattering spectra exhibit an unprecedented homogeneity, and the LBDP mode occurs at highly uniform positions with a very narrow standard deviation.[34] This is in stark contrast with the situation in nonideal dimers comprising the same gap distance (same linker molecule) but faceted building blocks: Here the LBDP position varies across many tens of nanometers due to the many different possibilities for the configuration of the crystal facets in the gap (different gap morphologies). A unique feature in dimers of noble-metal NPs with very short gaps (a few nanometers) is the occurrence of a hot spot upon resonant excitation, that is, a highly confined (a few cubic nanometers) volume with extremely high local electric fields (Figure 2). This hot spot can be exploited for highly sensitive vibrational spectroscopy of molecules located in the gap (single-molecule SERS).[35,36] The very high electric fields can also be exploited for driving chemical reactions[37] or for the efficient generation of hot carriers such as hot electrons, which can be transferred to adjacent semiconductors or molecular adsorbates (electron-transfer reaction).

Techniques of conventional optical microscopy cannot fully spatially resolve the hot spot due to the optical diffraction limit. Resolving the hot spot in a dimer with nanometer resolution can, however, be achieved with electron microscopy. In this case, the plasmon-induced nonequilibrium dynamics is probed by an optical probe pulse, which in a multiphoton transition leads to the ejection of detectable electrons. Specifically, we demonstrate the use of nonlinear photoemission electron microscopy (PEEM) for localizing hot spots in dimers of AuNSs with high spatial resolution after ultrafast optical excitation. Furthermore, we demonstrate that in addition to the highly uniform elastic scattering spectra, the hot spot in two different ideal dimers is highly uniform. Overall, these initial results are highly encouraging because they demonstrate the feasibility of precision plasmonics of single ideal colloidal particles at the limits of time (femtosecond electron diffraction) and space (PEEM) after ultrafast optical excitation.

2. MONOMERIC SPHERICAL GOLD NANOPARTICLES

In this section, we discuss experiments that investigate the final step of the nonradiative relaxation channel in laser-irradiated NPs, namely, the transfer of energy from the *hot* electronic system (after the decay of plasmonic excitations) to the lattice.

We use deposited films of monodisperse highly spherical AuNSs as samples, which removes inhomogeneous broadening effects in the corresponding optical spectrum of the particle film as well as in its structural response. The synthesis of the AuNSs is done by a seed-mediated growth method, where cetyltrimethylammonium bromide (CTAB) is employed as the stabilizing agent. In the last step of the synthesis, the obtained icosahedral NPs are etched by mild oxidation with tetrachloroauric(III) acid ($HAuCl_4$).[38] The resulting particles are round because the gold atoms with high-order facets have been removed. The size of the AuNSs can be controlled by the ratio of the concentration of the seed particles to the concentration of $HAuCl_4$ and the reducing agent.[39] Figure 3 (left) shows the transmission electron microscopy (TEM) images of ca. 50 nm and ca. 80 nm large AuNSs, demonstrating that the particles exhibit a high degree of monodispersity and roundness. The dynamic light scattering (DLS) data in Figure 3 (right) (hydrodynamic radius of ca. 31 nm and ca. 42 nm, respectively) and the corresponding UV−vis extinction spectra in Figure 3 (middle) (plasmon peak centered at ca. 528 and 542 nm) both indicate a narrow size distribution for the AuNSs dispersed in water. Because of the use of CTAB as the detergent with a positively charged quaternary ammonium group, the AuNSs show a positive zeta potential (11.6 and 5.6 mV).

The structural response of such AuNSs has been investigated by ultrafast time-resolved electron diffraction. For this purpose, 50 nm AuNSs have been deposited onto a 20 nm thick Si_3N_4 membrane in a Si wafer frame with a coverage of ∼0.05.

Experiments were carried out at the MeV ultrafast electron diffraction (UED) facility at SLAC National Accelerator Laboratory.[40] UED@SLAC employs a femtosecond laser-driven radio-frequency (RF) photogun and provides ultrashort electron pulses at relativistic energies. Here we used pulses of a few times 10^5 electrons per pulse, 200 fs fwhm bunch duration,

and 3.7 MeV kinetic energy at a repetition rate of 120 Hz. Using a normal incidence transmission geometry (see schematic in Figure 4a) the diffraction patterns were recorded by a single-electron-sensitive area detector, which was placed 3.5 m away from the sample, providing a momentum resolution of ~0.14 Å^{-1}.

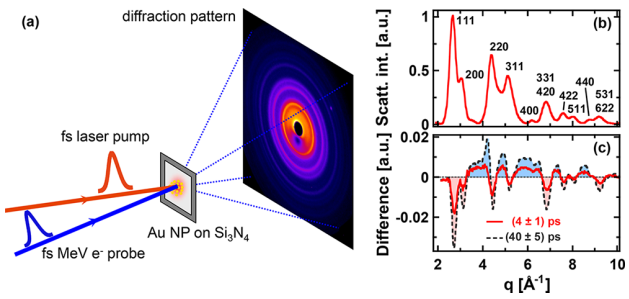

Figure 4. (a) Schematic of the experimental geometry. Spherical Au NPs of (50 ± 2.5) nm diameter deposited on 20 nm Si_3N_4 membranes are irradiated with 60 fs, 400 nm laser pulses (near-normal incidence). Their structural response is probed by diffraction of 200 fs, 3.7 MeV kinetic energy electron pulses in normal incidence transmission geometry. (b) Scattering intensity $I(q)$ of the unpumped sample as a function of momentum transfer. (c) Difference scattering pattern for delay times Δt = 4 ps (red) and Δt = 40 ps (black) after laser excitation (F = 6.3 mJ/cm^2).

For the time-resolved experiments, the frequency-doubled output (wavelength, 400 nm; pulse duration, 60 fs fwhm) of the Ti:sapphire laser that drives the photogun is used for sample excitation in a quasi-collinear geometry (angle of incidence, 3°). Both the optical pump pulse as well as the electron probe pulse (by a solenoid) were focused onto the sample to spot sizes of about 400 and 200 μm (fwhm), respectively.

Figure 4b shows the background-corrected scattering signal $I(q)$ of the nonexcited sample as a function of momentum transfer $q \approx 2\pi/\lambda \cdot \theta$ (λ = 0.003 Å: de Broglie wavelength, θ: scattering angle) obtained by azimuthal integration (along lines of constant q) of the diffraction pattern recorded by the area detector. All observed diffraction peaks correspond to the known reflections of Au (labeled by their corresponding Miller indices).

Upon optical excitation, the diffraction intensity changes, as can be seen in Figure 4c, showing a transient difference scattering pattern $\Delta I(q, \Delta t) = I(q, \Delta t) - I_0(q)$ ($I_0(q)$: unpumped) for time delays Δt of 4 (red) and 40 ps (black-dashed), respectively, at an excitation fluence F = 6.3 mJ/cm^2. A time-dependent decrease in the Bragg peak intensities as well as an increase in the diffuse background between the peaks can be recognized. As will be discussed in detail later, both features can be (mainly) attributed to the increase in the root-mean-square (rms) atomic displacement in the Au NPs after optical excitation.

For a quantitative analysis, the integrated signal of those Bragg peaks, which are either sufficiently strong or well separated from other peaks, has been determined through fitting with a Gaussian function superimposed on a (linear) background for each pump–probe time delay Δt. As a result, Figure 5a shows the integrated diffraction efficiency for several Bragg peaks for the same pump fluence of F = 6.3 mJ/cm^2 as in Figure 4c. The diffraction signal has been normalized to the value measured at negative delay times, that is, before sample excitation. As violet data points, Figure 5a also depicts the time dependence of the diffuse scattering signal measured between the (200) and (220) reflections from 3.5 to 3.9 Å^{-1}.

Whereas the different Bragg peaks exhibit an order-dependent decrease within a few picoseconds, the diffuse scattering intensity increases on similar time scales. This can be attributed to the transient Debye–Waller (DW) effect. Within the DW model, the intensity decrease in Bragg peaks $I_{hkl}(\Delta t)$ is caused by the increase in the rms atomic displacement $\Delta\langle u^2\rangle(\Delta t)$ and can be expressed as

$$I_{hkl}(\Delta t) = I^0_{hkl} \cdot e^{-1/3 G^2_{hkl} \Delta\langle u^2\rangle(\Delta t)} \Leftrightarrow$$
$$-\ln\left(\frac{I_{hkl}(\Delta t)}{I^0_{hkl}}\right) = \frac{1}{3} G^2_{hkl} \cdot \Delta\langle u^2\rangle(\Delta t) \quad (1)$$

Herein I^0_{hkl} denotes the scattering signal measured at negative time delays and G_{hkl} is the length of the reciprocal lattice vector corresponding to reflection (hkl). Whereas our experiment is only sensitive to the atomic motion parallel to the surface of the Si_3N_4 membranes used as substrates due to the normal-incidence geometry and the very short de Broglie wavelength (i.e., extremely flat Ewald sphere), we assume with eq 1 an isotropic response. This assumption is justified here because Au is an isotropic material and the particles are deposited with random orientation but can be violated for anisotropic materials and textured samples.[22]

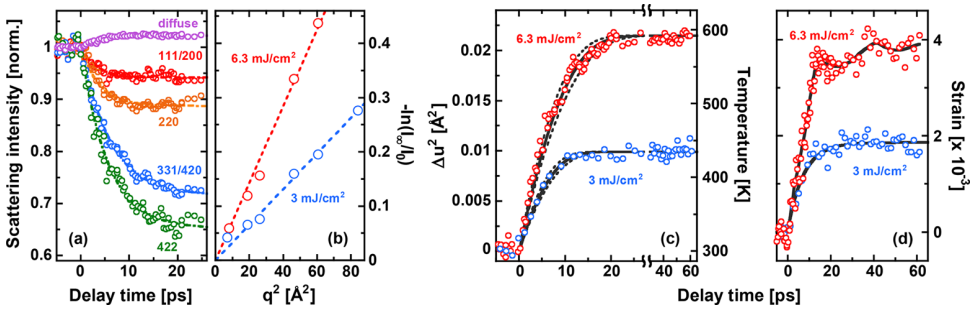

Figure 5. (a) Normalized integrated diffraction efficiency of various Bragg peaks (hkl) as a function of pump–probe time delay. The violet data points show the diffuse scattering signal measured at q = (3.7 ± 0.2) Å^{-1}. Pump fluence F = 6.3 mJ/cm^2. (b) *Asymptotic* logarithmic intensity change (averaged from 40 ≤ Δt ≤ 60 ps) as a function of G^2_{hkl}. (c) Change of the rms atomic displacement as a function of pump–probe time delay (right ordinate: derived lattice temperature); the black solid and dashed curves represent the results of calculations based on the two-temperature model for different electron–phonon coupling parameters (see eq 2). (d) Strain as a function of pump–probe time delay; black curves represent a guide to the eye. In panels b–d, blue and red data points represent experimental results for F = 3 and 6.3 mJ/cm^2, respectively.

The logarithmic form of the DW equation is particularly useful to verify whether the structural response is incoherent and can be described solely by the increase in the rms atomic displacement: Plotting the negative logarithm of the normalized intensity as a function of G_{hkl}^2 should result in a linear dependence with a slope determined by $\Delta\langle u^2\rangle$. Figure 5b shows these dependencies for the *asymptotic* intensity I_∞ (signal averaged over the delay range $40 \le \Delta t \le 60$ ps) as a function of G_{hkl}^2 for pump fluences $F = 3$ mJ/cm^2 (blue) and $F = 6.3$ mJ/cm^2 (red), respectively. The measured data indeed follow the linear behavior expected from the DW model, indicating that the lattice response is dominated by incoherent, statistical atomic motion. We verified that the DW model describes the experimental data for all delay times; therefore, the diffraction data can be used to determine $\Delta\langle u^2\rangle$ as a function of delay time, as shown in Figure 5c.

In a subsequent step, we used published data on the temperature dependence of the DW factor of Au[41,42] to convert the experimental $\Delta\langle u^2\rangle(\Delta t)$ into the transient temperature increase ΔT (Δt). The result of this conversion is shown in Figure 5c at the right ordinate, indicating that excitation at 3 and 6.3 mJ/cm^2 leads to a maximum temperature increase of 135 and 295 K, respectively.

We would like to stress that this conversion to temperature should, in principle, be treated with some care for two reasons: (i) Considerable and material-specific changes of the phonon spectrum (e.g., phonon softening[43−45]) can occur by electronic excitation, which effectively leads to a temporally varying Debye temperature of the material. Although phonon hardening has been predicted in the case of Au at very high electronic temperatures,[46] we do not expect such effects to be important at the excitation level of our experiment. (ii) Even for simple metals like Au, there is experimental[47,48] as well as theoretical[49] evidence that the phonon population generated through electronic relaxation is nonthermal for rather long time scales (i.e., tens of picoseconds). Thus the notion of a lattice temperature is, strictly speaking, not valid.

Being aware of these limitations, we nevertheless use the temperature concept to quantitatively analyze the energy flow in the system in the frame of the well-known two-temperature model[50] (TTM). The TTM assumes separate but thermalized distributions for electrons and phonons, respectively, and describes the response of the material by heat diffusion equations for the two subsystems coupled through the electron−phonon coupling parameter g. Additionally, we assume a spatially homogeneous deposition of the optical energy into the electronic system because the ballistic range of excited electrons in Au of ∼100 nm[51,52] is larger than the particle diameter. Because of the short pump pulse duration and the few picoseconds time scale of interest (as revealed by the experimental data), an instantaneous and homogenous increase in the electronic temperature was chosen as the starting condition instead of an explicit laser source term. This results in the following only time-dependent equation

$$-c_e\frac{\partial T_e}{\partial t} = c_L\frac{\partial T_L}{\partial t} = g(T_e - T_L) \tag{2}$$

Herein c_e and c_L denote the electronic and lattice specific heat, respectively, and g is the electron−phonon coupling parameter. Given the simplified nature of this description we use $c_e = 67.6\,\mathrm{J/(m^3\,K^2)}\cdot T_e$ and a constant lattice specific heat $c_L = 2.5$ MJ/(m^3 K). The electron−phonon coupling parameter is assumed to be constant as well, but it is treated as a free parameter in the calculations. The solid and dashed black curves in Figure 5c represent the results of such calculations. From a comparison with the experimental data, we determine $g = 1.8 \times 10^{16}$ W/(m^3 K) (solid curve) with an error of $\Delta g = \pm 0.2 \times 10^{16}$ W/(m^3 K) (dashed curves). Within the accuracy of the experiment, this is in agreement with the value of $g = 1.7 \times 10^{16}$ W/(m^3 K) for bulk Au obtained from electron diffraction experiments on free-standing as well as supported thin-film Au samples[26,29] but is lower than the value we have measured for nanoporous Au.[29]

In the latter case, the observed 30% increase in the electron−phonon coupling strength has been attributed to the "spill-out" of conduction band electrons at the surface of the nanostructured material, which leads to a reduced screening of the core potential of atoms in the surface region and thus to stronger electron−ion interactions. This mechanism has been introduced by Arbouet et al.[11] to explain the results of time-resolved optical data on Au and Ag NPs, which provided evidence of a speed-up of the electronic relaxation with decreasing particle size. In particular, their data indicate that these effects become increasingly important for particle sizes below 15 nm. In line with these observations, we determine for the 50 nm particles studied here an electron−phonon coupling parameter very close to the value of bulk Au.

Besides the time-dependent reduction of the diffraction intensity, we also observed a shift of the peaks toward smaller diffraction angles. Whereas these shifts are relatively small (∼1 pixel on the area detector for the highest order reflections at $F = 6.3$ mJ/cm^2), they are strictly proportional to the length of the corresponding reciprocal lattice vector: $\Delta q_{hkl} = \eta \cdot G_{hkl}$. Therefore, the proportionality constant η can be directly associated with strain due to the expansion of the particle. As can be seen in the inset of Figure 5d, the strain exhibits a similar time dependence as the increase in the rms displacement, with slight indications of a small oscillatory contribution (the black dashed curves represent a guide to the eye) at the higher pump fluence. Such oscillatory behavior is actually expected and has been observed in many studies, for both thin films (e.g., refs 53 and 54) as well as NPs.[55,56] For spherical particles, it corresponds to radial acoustic "breathing", modes which are triggered by the impulsive laser-induced increase in stress/pressure.[57,58] The close correspondence between the temporal evolution of strain and rms atomic displacement as well as the small oscillation amplitude seem to indicate that the acoustic waves are strongly damped. However, the noise of the strain data prohibits a further analysis/interpretation of the oscillatory contribution, and we will therefore focus on the absolute magnitude of the overall strain.

For late time delays, we determine a strain of $(1.9 \pm 0.1) \times 10^{-3}$ and $(3.9 \pm 0.2) \times 10^{-3}$ for pump fluences of 3 and 6.3 mJ/cm^2, respectively. Taking into account that such small particles can expand freely in all dimensions on a picosecond time scale and using the known linear thermal expansion (temperature-dependent) of Au,[59] an asymptotic temperature increase of (135 ± 7) and (275 ± 15) K is obtained for the two fluences. This is consistent with the temperature directly derived from the $\Delta\langle u^2\rangle$ data, providing some justification to use a temperature approach for the quantitative analysis of our data.

In summary, time-resolved diffraction with femtosecond, relativistic electron pulses has been used to investigate the structural response of spherical Au NPs upon ultrafast laser excitation. From our data, we directly determine the transient increase in the rms atomic displacement and thus the temporal evolution of the lattice temperature during electron−lattice

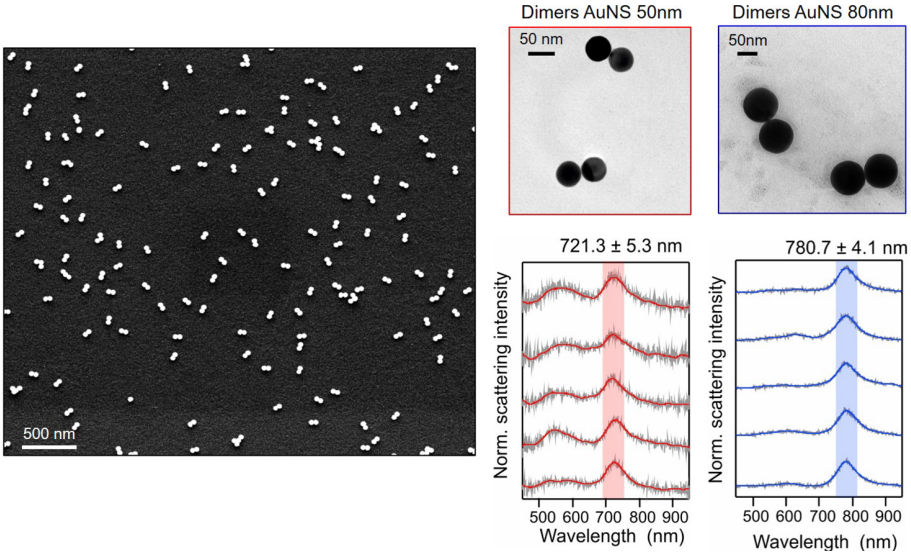

Figure 6. Characterization of ideal dimers by common techniques: SEM image of the ideal 50 nm AuNS dimers. (left) Comparison of TEM images of dimers with the same gap distance (1.3 nm) and different monomer sizes (50 and 80 nm) and their corresponding LSPR scattering spectra. (right) As evident from the image, an increase in the size of the constituent monomers leads to an efficient plasmonic coupling, leading to a red shift in the LBDP (bonding mode) band. The unprecedented uniformity in the structure is evident from the near-uniform position of LBDP bands for different dimers and their narrow standard deviations.

equilibration. Calculations based on the TTM using an electron–phonon coupling parameter $g = (1.8 \pm 0.2) \times 10^{16}$ W/(m^3 K) are in good agreement with the experiments. Furthermore, we observe the evolution of strain within a few picoseconds, which can be consistently interpreted as thermal expansion of the laser-heated NP. Our results demonstrate the possibilities of time-resolved diffraction for the study of plasmonic NPs.

3. IDEAL DIMERS OF SPHERICAL GOLD NANOPARTICLES

As discussed in the Introduction (Figure 2), dimers exhibit new plasmon modes due to plasmon hybridization and hot spots after resonant excitation of the LBDP mode along the dimer axis. The optical properties of dimers strongly depend on both the shape of the building blocks and their distance. Precision plasmonics on single dimers requires spherical building blocks assembled at small gap distances with angstrom resolution.

Ideal dimers of AuNSs can be synthesized by a solid-phase-supported approach. The first AuNS is deposited on a glass slide via electrostatic binding.[60] The CTAB bilayer of the adsorbed AuNS is destabilized by a combination of polar organic solvents (ethanol, acetonitrile) and sodium bromide.[61,62] The second AuNS is conjugated to the first AuNS by a linker molecule (alkyl dithiol).[63] Figure 6 shows (left) the scanning electron microscopy (SEM) image of ideal 50 nm AuNS dimers and (top-right) the TEM images of ideal dimers of AuNSs for different monomer sizes, 50 and 80 nm. The high yield of the synthesis (close to 90%) and the high uniformity of the ideal dimers are evident. The 50 nm AuNS dimers as well as the 80 nm AuNS dimers are bridged by 1,8-octanedithiol (C_8) molecules. Because of the high degree of geometrical uniformity, also the corresponding single-particle dark-field scattering spectra for both sizes are highly uniform, as shown in Figure 6 (bottom right). The peak at ca. 721 nm in the case of the 50 nm AuNS dimers is assigned to the LBDP-coupling mode. An increase in the size of the monomeric building block leads to a red shift in the LBDP band. As shown here, the assembly strategy also works equally well for larger AuNSs (e.g., 80 nm instead of 50 nm) and alkyl dithiol linkers with a different chain length (e.g., 1,10-decanedithiol (C_{10}) instead of C_8).[34]

None of the above-mentioned techniques provides insights into the local electric-field enhancement in the gap of the AuNS dimers. The direct visualization of these ultralow volume cavities was always off limits due to the optical diffraction limit. This fundamental problem can be overcome by using nonlinear photoelectron emission spectroscopy (PEEM), where we use electrons as the probe. Electrons with their subnanometer wavelength can provide us with the spatial resolution that is required to probe the gap distance on the order of a few angstroms.

The ideal dimer system consisting of two 80 nm AuNS separated by a gap distance of ~1.5 nm is used in the PEEM studies. The PEEM experiments were performed in ultrahigh vacuum (UHV) using a spectroscopic photoemission low-energy electron microscope (SPE-LEEM) made by Elmitec. The microscope was primarily used in three different operation modes.

First, the particles were located using threshold PEEM; that is, the surface was illuminated with ultraviolet light from a Hg discharge lamp, and the emitted electrons were used to form an image in the microscope. Examples for PEEM images of dimers and quadrumers are given in Figure 7a,b, respectively. The electron optical resolution of the SPE-LEEM is ~11 nm, and the PEEM images of the dimers and the quadrumers show the typical blurring that is common in threshold PEEM. Still, the individual local intensity maxima correspond to the number of particles in the oligomer. If more detailed information about the arrangement of the particles is desired, then the second method used in our study comes into play. Using an electron beam of an energy where the electrons are reflected at the surface potential (mirror electron microscopy (MEM)[64,65]) enhances the contrast at the edges of the particles. Figures 7c,d show MEM images of the same oligomers that were previously imaged with

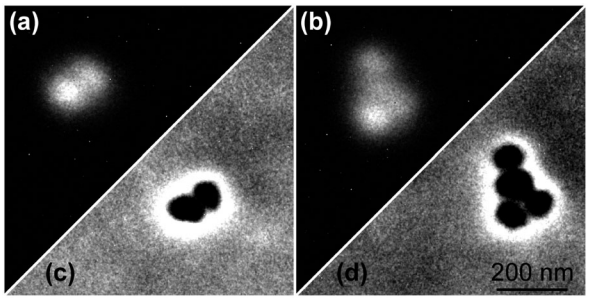

Figure 7. Au-particle-based oligomers. (a,b) Threshold PEEM images of a dimer and a quadrumer showing the bright particles, as they emit more photoelectrons than the surrounding substrate. (c,d) MEM images of the same oligomers as in panels a and b, respectively. The particles appear black with a white halo. The particles comprising the oligomers have a diameter of ~80 nm.

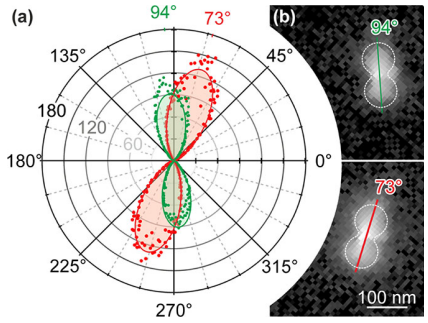

Figure 8. Polarization dependence of the emission characteristics. (a) Electron emission yield of the two dimers shown in panel b as a function of polarization angle. The electron emission yield of the two dimers shows a maximum whenever the polarization is aligned with the long axis of the dimer. The solid lines are fits following a fourth-order emission process.

threshold PEEM. In the MEM images, the immediate vicinity of the particles appears bright, whereas the particles themselves are imaged dark. From the transition of black to white regions across the particle, we can estimate the approximate particle size to be 80 nm. The contrast is also strong enough to count the particles in the oligomer and to determine their arrangement. Whereas this is less important for the dimer, we can conclude for the quadrumer that it is composed of two pairs of dimers that comprise an angle of their long axis of roughly 80°. In the following, we will focus on the analysis of dimers only.

To investigate the optical polarization sensitivity of the plasmon resonances, we use nonlinear photoemission microscopy (nPPE PEEM).[66] For this experiment, the microscope is combined with a Ti:sapphire laser system (FEMTOLASERS) delivering femtosecond laser pulses that impinge on the sample surface along the surface normal.[67] The relevant parameters of the laser pulses are their central wavelength of 800 nm (E_{ph} = 1.55 eV), a pulse duration of ≤15 fs, and a pulse energy of ~1 nJ. The general optical setup has been previously described.[68,69] For the work presented here, it is important to emphasize that we can adjust the pulse energy at the sample by using a zero-order $\lambda/2$-waveplate to rotate the polarization direction and combine it with a reflection at a glass plate under the Brewster angle. Behind this Brewster reflector, we obtain an s-polarized beam with adjustable intensity. Using a second zero-order $\lambda/2$-waveplate, we can then rotate the linear polarization direction to any orientation within the surface plane. The combination of the Brewster reflector with the two waveplates allows us to adjust the intensity and the polarization independently.

We will now discuss the nPPE results in Figure 8. Two different dimers that were selected and analyzed are shown in the top and bottom of Figure 8b. By design, the dimers were fabricated to exhibit a resonant gap mode[70,71] at 800 nm. The highest electron yield is found in the region of the gap between the particles comprising the dimer,[71,72] reflecting the high electrical-field enhancement there.[73−76] If the polarization is rotated, then the electron yield will vary because the electron emission from the gap is strongly polarization-dependent. Figure 8a analyzes the polarization dependence for the two dimers in panel b in 1° steps. More specifically, the green data points correspond to the dimer in the top of Figure 8b, whereas the red data points correspond to the dimer in the bottom of that panel. The radial coordinate in Figure 8a is proportional to the detected electron yield, whereas the azimuthal coordinate describes the polarization angle on the equator of the Poincaré sphere. The electron emission from the two dimers exhibits distinct maxima at particular polarization angles where the gap mode can be efficiently excited. This is the case whenever the polarization is aligned with the long axis of the dimer. Following this argument, we can determine the orientation of the dimers on the surface with high precision. The two dimers that we analyzed are apparently rotated with respect to each other by 21°.

The green and red solid lines in Figure 8a are numerical fits through the data $Y(\vartheta) \propto \cos^{2n}(\vartheta)$ with $Y(\vartheta)$ for the measured electron yield and ϑ for the polarization angle. The fit parameter n indicates the order of the nonlinear electron emission process. For the case of the two dimers discussed here, we find values for $n \approx 4$, which indicates that four quanta from the superposition of the laser's electric field and the plasmonic resonance are necessary to emit one electron. The particles' surfaces are thus sufficiently clean to maintain the high work function of pristine Au of 5.3 eV, and all lower nonlinear emission processes are suppressed. Also, in Figure 8a, the maximum electron emission yield from the dimer in panel b corresponding to the green data points amounts to only ~70% of the one from the dimer in panel c with red data points. Considering the nonlinear character of the emission process, however, the 30% lower electron emission translates into a difference in field enhancement of only 9%. Apparently, the field-enhancement characteristics of the two dimers are very similar.

Figure 9 shows an analysis of the emission yield of two different dimers as a function of the overall average laser power. The two dimers are again indicated by red and green data points, and nPPE PEEM images of the dimers are shown as insets. The yield on the ordinate of Figure 9 corresponds to the integral intensity of a region of interest placed on the dimer. The polarization was adjusted and then fixed to achieve roughly comparable emission yields from both dimers. In the double-logarithmic representation, the nonlinear emission is represented by lines following a power law $Y(P) = P^n$; that is, from the slope of the lines, we can extract the order of the emission process n with great accuracy. For the dimer marked in red, we find n = 4.0, consistent with the analysis in the polar plot (Figure 8). The dimer with the green frame in Figure 9 shows n = 4.4, which seems surprising because it suggests a fractional number of energy quanta to be absorbed during the emission of each electron. On the basis of our previous work on nonlinear

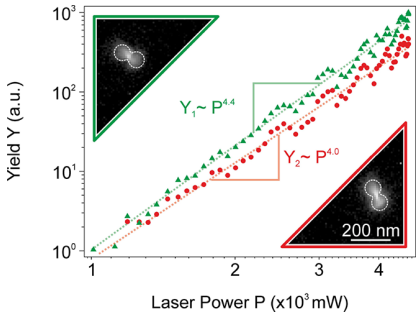

Figure 9. Laser-power dependence of the nonlinear electron emission yield for the two dimers shown in the insets. The order of the emission process can be determined from the slope of the lines in the double-logarithmic plot.

plasmoemission,[77] we know that in nonlinear electron emission from plasmons, several emission pathways can exist in parallel. If the field enhancement is high enough, then not only a fourth-order process but also a fifth-order process will become possible. Because the data presented here is not energy-filtered, both emission pathways will contribute to the yield, and any contribution from a fifth-order (or higher) process will push the measured value for n above $n = 4$. The explanation is consistent with the finding $n = 4$ for the particle with the red frame, as the overall emission yield of that particle is smaller, and the fifth-order process will play a lesser role.

Linear and nonlinear photoemission microscopy in combination with mirror electron microscopy were used to investigate oligomers composed of self-assembled Au particles. In the microscope, we can clearly identify the size of the particles and their arrangement. Most of the oligomers are dimers, and they exhibit substantial electrical-field enhancement due to the plasmonic mode formed in the gap between the particles. In nonlinear photoemission microscopy, we can visualize that the strongest field is indeed localized in the gap, and the nonlinear character of the fourth-order electron emission mechanism is an indication of the substantial field enhancement at this position. We observe the expected polarization dependence; that is, the gap mode is excited when the light's polarization vector is aligned with the long axis of the dimer. By rotating the polarization direction and by comparing the maximal photoemission yield from two different dimers, we find that the electric fields in the gap of the two dimers differ by only ~9%. On the basis of this analysis, we conclude that the self-assembly method used to produce the dimers yields a very defined and reproducible gap.

4. OUTLOOK

Chemists are nowadays able to synthesize highly spherical gold NPs and to assemble them into well-defined structures such as dimers with well-defined short gaps and distance control at the angstrom level. This uniformity and reproducibility across a set of single colloidal particles (monomers and dimers) is expressed by the term precision plasmonics. Optical spectroscopy, however, is generally limited in terms of both its structural information content (because it typically probes the electronic system and not the lattice) and its spatial resolution (diffraction limit). These drawbacks can be overcome by using electrons to interrogate plasmonic systems at the time and space limits. By directly probing the nonequilibrium lattice dynamics by femtosecond electron diffraction after ultrafast optical excitation, researchers are nowadays able to monitor the evolution of stress and heat in plasmonic nanostructures in the time domain. This provides fundamentals insight into the coupling between the electronic system and the metal lattice in the spatially confined dimensions of a noble-metal NP, which is physically different from the situation in an extended metal film. The extremely high electric fields generated upon ultrafast optical excitation can induce the efficient generation of hot carriers such as hot electrons, which, in turn, can be extracted to adjacent electron acceptors (semiconductors, molecules) for solar to chemical energy conversion. Probing these enhanced local electric fields by femtosecond nonlinear PEEM on the nanoscale provides unique insights into the electronic response of the system after ultrafast optical excitation. Beyond the impact of these techniques on purely metallic nanostructures, one can also easily envision numerous fundamental studies in molecular precision plasmonics, where metal/molecule interfaces are present in hybrid structures. Exploiting, for example, the highly uniform gap and, in particular, the extreme field enhancement in the gap will pave the way toward precision SERS where molecules located in the gaps of ideal dimers will ideally show highly comparable SERS intensities from single dimer to single dimer. Overall, these initial results on monomers and dimers of spherical gold NPs presented in this Feature Article are highly encouraging because they demonstrate the feasibility of precision plasmonics of single ideal colloidal particles at the limits of time and space after ultrafast optical excitation.

AUTHOR INFORMATION

Corresponding Authors

*F.M.z.H.: E-mail: meyerzh@uni-due.de.
*K.S.-T.: E-mail: Klaus.Sokolowski-Tinten@uni-due.de.
*S.S.: E-mail: sebastian.schluecker@uni-due.de.

ORCID

T. J. Davis: 0000-0002-7299-4900
F. Meyer zu Heringdorf: 0000-0002-5878-2012
S. Schlücker: 0000-0003-4790-4616

Present Address

[‖]T.J.D.: School of Physics, University of Melbourne, Parkville 3010, Australia.

Notes

The authors declare no competing financial interest.

Biographies

Frank Meyer zu Heringdorf is a professor at the University of Duisburg-Essen and a member of the Centre for Nanointegration Duisburg-Essen (CENIDE). He received his Ph.D. in physics with honors from the University of Hannover (Germany) in 1999 and then joined IBM's

research center in Yorktown Heights as a postdoctoral Feodor-Lynen Fellow. He then established time-resolved photoemission microscopy as a new method at the University of Essen and obtained his habilitation there in 2010 for a thesis on his microscopy work. He was awarded the Gottschalk-Diederich-Baedeker prize in 2011. Frank's research interests still include low-energy electron microscopy and time-resolved photoemission microscopy with an emphasis on nanoscience and surface plasmons.

Photo provided by Andreas Reichert

Klaus Sokolowsi-Tinten is a Senior Staff Scientist and Adjunct Professor at the Faculty of Physics of the Universität Duisburg-Essen and a member of the CENIDE (Center for Nanointegration Duisburg-Essen). He obtained his Diploma and Ph.D. in physics at the Universität Gesamthochschule Essen. His main research interests are in the field of ultrafast laser–material interactions, with particular emphasis on the investigation of the structural dynamics under strongly nonequilibrium conditions using advanced time-resolved scattering techniques with femtosecond X-ray and electron pulses.

Sebastian Schlücker is a Professor of Physical Chemistry at the University Duisburg-Essen and a member of the Center for Nano-integration Duisburg-Essen (CENIDE). He received his diploma and Dr. rer. nat. (Ph.D.) in chemistry from the University of Würzburg in 2002 and completed postdoctoral training at the NIH in Bethesda, MD. His research interests are the physics and chemistry of molecularly functionalized plasmonic nanostructures and their application in biomedicine and energy conversion. In 2018, he founded NanoWerke GmbH.

ACKNOWLEDGMENTS

This work is funded by the Deutsche Forschungsgemeinschaft (DFG, German Research Foundation) - Projektnummer 278162697 - SFB 1242 "non-equilibrium dynamics of condensed matter in the time domain" (A04, B06, C01). The UED work was performed at SLAC MeV-UED, which is supported in part by the DOE BES SUF Division Accelerator & Detector R&D program, the LCLS Facility, and SLAC under contract nos. (DE-AC02-05-CH11231) and (DE-AC02-76SF00515). L.S. and S.S. acknowledge financial support from Evonik Industries for a Ph.D. fellowship for L.S.

REFERENCES

(1) Brongersma, M. L.; Halas, N. J.; Nordlander, P. Plasmon-induced Hot Carrier Science and Technology. *Nat. Nanotechnol.* **2015**, *10*, 25–34.

(2) Grimvall, G. *The Electron-Phonon Interaction in Metals*; Series of Monographs on Selected Topics in Solid State Physics *XVI*; North-Holland Pub. Co.: Amsterdam, The Netherlands, 1981.

(3) Willets, K. A.; Van Duyne, R. P. Localized Surface Plasmon Resonance Spectroscopy and Sensing. *Annu. Rev. Phys. Chem.* **2007**, *58*, 267–297.

(4) Schlücker, S. Surface-Enhanced Raman Spectroscopy: Concepts and Chemical Applications. *Angew. Chem., Int. Ed.* **2014**, *53*, 4756–4795.

(5) Clavero, C. Plasmon-induced Hot-Electron Generation at Nanoparticle/Metal-oxide Interfaces for Photovoltaic and Photocatalytic Devices. *Nat. Photonics* **2014**, *8*, 95–103.

(6) Linic, S.; Aslam, U.; Boerigter, C.; Morabito, M. Photochemical Transformations on Plasmonic Metal Nanoparticles. *Nat. Mater.* **2015**, *14*, 567–576.

(7) Cortés, E.; Xie, W.; Cambiasso, J.; Jermyn, A. S.; Sundararaman, R.; Narang, P.; Schlücker, S.; Maier, S. A. Plasmonic Hot Electron Transport Drives Nano-localized Chemistry. *Nat. Commun.* **2017**, *8*, 14880.

(8) Zhang, X.; Li, X.; Reish, M. E.; Zhang, D.; Su, N. Q.; Gutiérrez, Y.; Moreno, F.; Yang, W.; Everitt, H. O.; Liu, J. Plasmon-Enhanced Catalysis: Distinguishing Thermal and Nonthermal Effects. *Nano Lett.* **2018**, *18*, 1714–1723.

(9) Zhou, L.; Swearer, D. F.; Zhang, C.; Robatjazi, H.; Zhao, H.; Henderson, L.; Dong, L.; Christopher, P.; Carter, E. A.; Nordlander, P.; et al. Quantifying Hot Carrier and Thermal Contributions in Plasmonic Photocatalysis. *Science* **2018**, *362*, 69–72.

(10) Baffou, G.; Quidant, R. Thermo-plasmonics: Using Metallic Nanostructures as Nano-sources of Heat. *Laser Photonics Rev.* **2013**, *7*, 171–187.

(11) Arbouet, A.; Voisin, C.; Christofilos, D.; Langot, P.; Fatti, N. D.; Vallée, F.; Lermé, J.; Celep, G.; Cottancin, E.; Gaudry, M.; et al. Electron-Phonon Scattering in Metal Clusters. *Phys. Rev. Lett.* **2003**, *90*, 177401.

(12) Yu, S.; Zhang, J.; Tang, Y.; Ouyang, M. Engineering Acoustic Phonons and Electron-Phonon Coupling by the Nanoscale Interface. *Nano Lett.* **2015**, *15*, 6282–6288.

(13) Hartland, G. V. Optical Studies of Dynamics in Noble Metal Nanostructures. *Chem. Rev.* **2011**, *111*, 3858–3887.

(14) Plech, A.; Kotaidis, V.; Lorenc, M.; Boneberg, J. Femtosecond Laser Near-field Ablation from Gold Nanoparticles. *Nat. Phys.* **2006**, *2*, 44–47.

(15) Nie, S.; Wang, X.; Park, H.; Clinite, R.; Cao, J. Measurement of the Electronic Grüneisen Constant Using Femtosecond Electron Diffraction. *Phys. Rev. Lett.* **2006**, *96*, 025901.

(16) Ruan, C.-Y.; Murooka, Y.; Raman, R. K.; Murdick, R. A. Dynamics of Size-Selected Gold Nanoparticles Studied by Ultrafast Electron Nanocrystallography. *Nano Lett.* **2007**, *7*, 1290–1296.

(17) Ernstorfer, R.; Harb, M.; Hebeisen, C. T.; Sciaini, G.; Dartigalongue, T.; Miller, R. J. D. The Formation of Warm Dense Matter: Experimental Evidence for Electronic Bond Hardening in Gold. *Science* **2009**, *323*, 1033–1037.

(18) Liang, W.; Schäfer, S.; Zewail, A. H. Ultrafast Electron Crystallography of Heterogeneous Structures: Gold-graphene Bilayer and Ligand-encapsulated Nanogold on Graphene. *Chem. Phys. Lett.* **2012**, *542*, 8–12.

(19) Clark, J. N.; Beitra, L.; Xiong, G.; Higginbotham, A.; Fritz, D. M.; Lemke, H. T.; Zhu, D.; Chollet, M.; Williams, G. J.; Messerschmidt, M.; et al. Ultrafast Three-Dimensional Imaging of Lattice Dynamics in Individual Gold Nanocrystals. *Science* **2013**, *341*, 56−59.
(20) Frigge, T.; Hafke, B.; Tinnemann, V.; Krenzer, B.; Horn-von Hoegen, M. Nanoscale Heat Transport from Ge Hut, Dome, and Relaxed Clusters on Si(001) Measured by Ultrafast Electron Ddiffraction. *Appl. Phys. Lett.* **2015**, *106*, 053108.
(21) Szilagyi, E.; Wittenberg, J. S.; Miller, T. A.; Lutker, K.; Quirin, F.; Lemke, H.; Zhu, D.; Chollet, M.; Robinson, J.; Wen, H.; et al. Visualization of Nanocrystal Breathing Modes at Extreme Strains. *Nat. Commun.* **2015**, *6*, 6577.
(22) Sokolowski-Tinten, K.; Li, R. K.; Reid, A. H.; Weathersby, S. P.; Quirin, F.; Chase, T.; Coffee, R.; Corbett, J.; Fry, A.; Hartmann, N.; et al. Thickness-dependent Electron−lattice Equilibration in Laser-excited Thin Bismuth Films. *New J. Phys.* **2015**, *17*, 113047.
(23) Valley, D. T.; Ferry, V. E.; Flannigan, D. J. Imaging Intra- and Interparticle Acousto-plasmonic Vibrational Dynamics with Ultrafast Electron Microscopy. *Nano Lett.* **2016**, *16*, 7302−7308.
(24) Ferguson, K. R.; Bucher, M.; Gorkhover, T.; Boutet, S.; Fukuzawa, H.; Koglin, J. E.; Kumagai, Y.; Lutman, A.; Marinelli, A.; Messerschmidt, M.; et al. Transient Lattice Contraction in the Solid-to-plasma Ttransition. *Sci. Adv.* **2016**, *2*, e1500837.
(25) Mancini, G. F.; Latychevskaia, T.; Pennacchio, F.; Reguera, J.; Stellacci, F.; Carbone, F. Order/Disorder Dynamics in a Dodecanethiol-Capped Gold Nanoparticles Supracrystal by Small-Angle Ultrafast Electron Diffraction. *Nano Lett.* **2016**, *16*, 2705−2713.
(26) Sokolowski-Tinten, K.; Shen, X.; Zheng, Q.; Chase, T.; Coffee, R.; Jerman, M.; Li, R. K.; Ligges, M.; Makasyuk, I.; Mo, M.; et al. Electron-lattice Energy Relaxation in Laser-excited Thin-film Au-insulator Heterostructures Studied by Ultrafast MeV Electron Diffraction. *Struct. Dyn.* **2017**, *4*, 054501.
(27) Frigge, T.; Hafke, B.; Witte, T.; Krenzer, B.; Streubühr, C.; Samad Syed, A.; Mikšić Trontl, V.; Avigo, I.; Zhou, P.; Ligges, M.; et al. Optically Excited Structural Transition in Atomic Wires on Surfaces at the Quantum Limit. *Nature* **2017**, *544*, 207−211.
(28) Reid, A. H.; Shen, X.; Maldonado, P.; Chase, T.; Jal, E.; Granitzka, P. W.; Carva, K.; Li, R. K.; Li, J.; Wu, L.; et al. Publisher Correction: Beyond a phenomenological Description of Magnetostriction. *Nat. Commun.* **2018**, *9*, 1035.
(29) Zheng, Q.; Shen, X.; Sokolowski-Tinten, K.; Li, R. K.; Chen, Z.; Mo, M. Z.; Wang, Z. L.; Weathersby, S. P.; Yang, J.; Chen, M. W.; et al. Dynamics of Electron−Phonon Coupling in Bicontinuous Nanoporous Gold. *J. Phys. Chem. C* **2018**, *122*, 16368−16373.
(30) Mo, M. Z.; Chen, Z.; Li, R. K.; Dunning, M.; Witte, B. B. L.; Baldwin, J. K.; Fletcher, L. B.; Kim, J. B.; Ng, A.; Redmer, R.; et al. Heterogeneous to homogeneous melting transition visualized with ultrafast electron diffraction. *Science* **2018**, *360*, 1451−1455.
(31) Vasileiadis, T.; Waldecker, L.; Foster, D.; Da Silva, A.; Zahn, D.; Bertoni, R.; Palmer, R. E.; Ernstorfer, R. Ultrafast Heat Flow in Heterostructures of Au Nanoclusters on Thin Films: Atomic Disorder Induced by Hot Electrons. *ACS Nano* **2018**, *12*, 7710−7720.
(32) Nordlander, P.; Oubre, C.; Prodan, E.; Li, K.; Stockman, M. I. Plasmon Hybridization in Nanoparticle Dimers. *Nano Lett.* **2004**, *4*, 899−903.
(33) Gersten, J. I.; Nitzan, A. Photophysics and photochemistry near surfaces and small particles. *Surf. Sci.* **1985**, *158*, 165−189.
(34) Yoon, J. H.; Selbach, F.; Langolf, L.; Schlücker, S. Ideal Dimers of Gold Nanospheres for Precision Plasmonics: Synthesis and Characterization at the Single-Particle Level for Identification of Higher Order Modes. *Small* **2018**, *14*, 1702754.
(35) Nie, S. Probing Single Molecules and Single Nanoparticles by Surface-Enhanced Raman Scattering. *Science* **1997**, *275*, 1102−1106.
(36) Kneipp, K.; Wang, Y.; Kneipp, H.; Perelman, L. T.; Itzkan, I.; Dasari, R. R.; Feld, M. S. Single Molecule Detection Using Surface-Enhanced Raman Scattering (SERS). *Phys. Rev. Lett.* **1997**, *78*, 1667−1670.
(37) Cortés, E. Activating Plasmonic Chemistry. *Science* **2018**, *362*, 28−29.
(38) Rodríguez-Fernández, J.; Pérez-Juste, J.; Mulvaney, P.; Liz-Marzán, L. M. Spatially-directed oxidation of gold nanoparticles by Au(III)-CTAB complexes. *J. Phys. Chem. B* **2005**, *109*, 14257−14261.
(39) Ruan, Q.; Shao, L.; Shu, Y.; Wang, J.; Wu, H. Growth of Monodisperse Gold Nanospheres with Diameters from 20 to 220 nm and Their Core/Satellite Nanostructures. *Adv. Opt. Mater.* **2014**, *2*, 65−73.
(40) Weathersby, S. P.; Brown, G.; Centurion, M.; Chase, T. F.; Coffee, R.; Corbett, J.; Eichner, J. P.; Frisch, J. C.; Fry, A. R.; Gühr, M.; et al. Mega-electron-volt Ultrafast Electron Diffraction at SLAC National Accelerator Laboratory. *Rev. Sci. Instrum.* **2015**, *86*, 073702.
(41) Syneček, V.; Chessin, H.; Simerska, M. The Temperature Dependence of Lattice Vibrations in Gold from X-ray Diffraction Measurements. *Acta Crystallogr., Sect. A: Cryst. Phys., Diffr., Theor. Gen. Crystallogr.* **1970**, *26*, 108−113.
(42) Gao, H. X.; Peng, L.-M. Parameterization of the Temperature Dependence of the Debye−Waller Factors. *Acta Crystallogr., Sect. A: Found. Crystallogr.* **1999**, *55*, 926−932.
(43) Murray, É. D.; Fahy, S.; Prendergast, D.; Ogitsu, T.; Fritz, D. M.; Reis, D. A. Phonon Dispersion Relations and Softening in Photoexcited Bismuth from First Principles. *Phys. Rev. B: Condens. Matter Mater. Phys.* **2007**, *75*, 184301.
(44) Sokolowski-Tinten, K.; Blome, C.; Blums, J.; Cavalleri, A.; Dietrich, C.; Tarasevitch, A.; Uschmann, I.; Förster, E.; Kammler, M.; Horn-von-Hoegen, M.; et al. Femtosecond X-ray Measurement of Coherent Lattice Vibrations Near the Lindemann Stability Limit. *Nature* **2003**, *422*, 287−289.
(45) Fritz, D. M.; Reis, D. A.; Adams, B.; Akre, R. A.; Arthur, J.; Blome, C.; Bucksbaum, P. H.; Cavalieri, A. L.; Engemann, S.; Fahy, S.; et al. Ultrafast Bond Softening in Bismuth: Mapping a Solid's Interatomic Potential with X-rays. *Science* **2007**, *315*, 633−636.
(46) Recoules, V.; Clérouin, J.; Zérah, G.; Anglade, P. M.; Mazevet, S. Effect of Intense Laser Irradiation on the Lattice Stability of Semiconductors and Metals. *Phys. Rev. Lett.* **2006**, *96*, 055503.
(47) Waldecker, L.; Bertoni, R.; Ernstorfer, R.; Vorberger, J. Electron-Phonon Coupling and Energy Flow in a Simple Metal beyond the Two-Temperature Approximation. *Phys. Rev. X* **2016**, *6*, 021003.
(48) Chase, T.; Trigo, M.; Reid, A. H.; Li, R.; Vecchione, T.; Shen, X.; Weathersby, S.; Coffee, R.; Hartmann, N.; Reis, D. A.; et al. Ultrafast Electron Diffraction from Non-equilibrium Phonons in Femtosecond Laser Heated Au Films. *Appl. Phys. Lett.* **2016**, *108*, 041909.
(49) Maldonado, P.; Carva, K.; Flammer, M.; Oppeneer, P. M. Theory of Out-of-equilibrium Ultrafast Relaxation Dynamics in Metals. *Phys. Rev. B: Condens. Matter Mater. Phys.* **2017**, *96*, 174439.
(50) Anisimov, S. I.; Kapeliovich, B. L.; Perelman, T. L. Electron Emission from Metal Surfaces Exposed to Ultrashort Laser Pulses. *J. Exp. Theor. Phys.* **1973**, *66*, 375−377.
(51) Brorson, S. D.; Fujimoto, J. G.; Ippen, E. P. Femtosecond Electronic Heat-transport Dynamics in Thin Gold Films. *Phys. Rev. Lett.* **1987**, *59*, 1962−1965.
(52) Hohlfeld, J.; Müller, J. G.; Wellershoff, S.-S.; Matthias, E. Time-resolved Thermoreflectivity of Thin Gold Films and its Dependence on Film Thickness. *Appl. Phys. B: Lasers Opt.* **1997**, *64*, 387−390.
(53) Park, H.; Wang, X.; Nie, S.; Clinite, R.; Cao, J. Mechanism of Coherent Acoustic Phonon Generation under Nonequilibrium Conditions. *Phys. Rev. B: Condens. Matter Mater. Phys.* **2005**, *72*, 100301.
(54) Nicoul, M.; Shymanovich, U.; Tarasevitch, A.; von der Linde, D.; Sokolowski-Tinten, K. Picosecond Acoustic Response of a Laser-heated Gold-film Studied with Time-resolved X-ray Diffraction. *Appl. Phys. Lett.* **2011**, *98*, 191902.
(55) Hartland, G. V. Coherent Excitation Of Vibrational Modes In Metallic Nanoparticles. *Annu. Rev. Phys. Chem.* **2006**, *57*, 403−430.
(56) Crut, A.; Maioli, P.; Del Fatti, N.; Vallée, F. Acoustic Vibrations Of Metal Nano-objects: Time-domain Investigations. *Phys. Rep.* **2015**, *549*, 1−43.
(57) Thomsen, C.; Grahn, H. T.; Maris, H. J.; Tauc, J. Surface Generation and Detection of Phonons by Picosecond Light Pulses. *Phys. Rev. B: Condens. Matter Mater. Phys.* **1986**, *34*, 4129−4138.

(58) Wright, O. B. Ultrafast Nonequilibrium Stress Generation in Gold and Silver. *Phys. Rev. B: Condens. Matter Mater. Phys.* **1994**, *49*, 9985−9988.
(59) Suh, I.-K.; Ohta, H.; Waseda, Y. High-temperature Thermal Expansion of Six Metallic Elements Measured by Dilatation Method and X-ray Diffraction. *J. Mater. Sci.* **1988**, *23*, 757−760.
(60) Guo, L.; Zhou, X.; Kim, D.-H. Facile Fabrication of Distance-tunable Au-nanorod Chips for Single-nanoparticle Plasmonic Biosensors. *Biosens. Bioelectron.* **2011**, *26*, 2246−2251.
(61) Liu, K.; Zheng, Y.; Lu, X.; Thai, T.; Lee, N. A.; Bach, U.; Gooding, J. J. Biocompatible Gold Nanorods: One-step Surface Functionalization, Highly Colloidal Stability, and Low Cytotoxicity. *Langmuir* **2015**, *31*, 4973−4980.
(62) Nepal, D.; Park, K.; Vaia, R. A. High-yield Assembly of Soluble and Stable Gold Nanorod Pairs for High-temperature Plasmonics. *Small* **2012**, *8*, 1013−1020.
(63) Cha, H.; Yoon, J. H.; Yoon, S. Probing Quantum Plasmon Coupling Using Gold Nanoparticle Dimers with Tunable Interparticle Distances Down to the Subnanometer Range. *ACS Nano* **2014**, *8*, 8554−8563.
(64) Orthuber, R. Über Die Anwendung Des Elektronenspiegels zum Abbilden der Potentialverteilung auf Metallischen und Halbleiteroberflächen. *Z. Angew. Phys.* **1948**, *1*, 79−89.
(65) Święch, W.; Rausenberger, B.; Engel, W.; Bradshaw, A. M.; Zeitler, E. In-situ Studies of Heterogeneous Reactions Using Mirror Electron Microscopy. *Surf. Sci.* **1993**, *294*, 297−307.
(66) Schmidt, O.; Bauer, M.; Wiemann, C.; Porath, R.; Scharte, M.; Andreyev, O.; Schönhense, G.; Aeschlimann, M. Time-resolved Two Photon Photoemission Electron Microscopy. *Appl. Phys. B: Lasers Opt.* **2002**, *74*, 223−227.
(67) Kahl, P.; Wall, S.; Witt, C.; Schneider, C.; Bayer, D.; Fischer, A.; Melchior, P.; Horn-von Hoegen, M.; Aeschlimann, M.; Meyer zu Heringdorf, F.-J. Normal-Incidence Photoemission Electron Microscopy (NI-PEEM) for Imaging Surface Plasmon Polaritons. *Plasmonics* **2014**, *9*, 1401−1407.
(68) Chelaru, L. I.; Horn-von Hoegen, M.; Thien, D.; Meyer zu Heringdorf, F.-J. Fringe Fields in Nonlinear Photoemission Microscopy. *Phys. Rev. B: Condens. Matter Mater. Phys.* **2006**, *73*, 115416.
(69) Meyer zu Heringdorf, F. J.; Podbiel, D.; Raß, N.; Makris, A.; Buckanie, N. M.; Kahl, P. A. Spatio-temporal Imaging of Surface Plasmon Polaritons in Two Photon Photoemission Microscopy. *Proc. SPIE* **2016**, 992110.
(70) Aćimović, S. S.; Kreuzer, M. P.; González, M. U.; Quidant, R. Plasmon Near-Field Coupling in Metal Dimers as a Step toward Single-Molecule Sensing. *ACS Nano* **2009**, *3*, 1231−1237.
(71) Rechberger, W.; Hohenau, A.; Leitner, A.; Krenn, J. R.; Lamprecht, B.; Aussenegg, F. R. Optical Properties of Two Interacting Gold Nanoparticles. *Opt. Commun.* **2003**, *220*, 137−141.
(72) Hatab, N. A.; Hsueh, C.-H.; Gaddis, A. L.; Retterer, S. T.; Li, J.-H.; Eres, G.; Zhang, Z.; Gu, B. Free-Standing Optical Gold Bowtie Nanoantenna with Variable Gap Size for Enhanced Raman Spectroscopy. *Nano Lett.* **2010**, *10*, 4952−4955.
(73) Douillard, L.; Charra, F.; Fiorini, C.; Adam, P. M.; Bachelot, R.; Kostcheev, S.; Lerondel, G.; Lamy de la Chapelle, M.; Royer, P. Optical Properties of Metal Nanoparticles as Probed by Photoemission Electron Microscopy. *J. Appl. Phys.* **2007**, *101*, 083518.
(74) Bayer, D.; Wiemann, C.; Gaier, O.; Bauer, M.; Aeschlimann, M. Time-Resolved 2PPE and Time-Resolved PEEM as a Probe of LSP's in Silver Nanoparticles. *J. Nanomater.* **2008**, *2008*, 1−11.
(75) Schertz, F.; Schmelzeisen, M.; Mohammadi, R.; Kreiter, M.; Elmers, H.-J.; Schönhense, G. Near Field of Strongly Coupled Plasmons: Uncovering Dark Modes. *Nano Lett.* **2012**, *12*, 1885−1890.
(76) Sun, Q.; Ueno, K.; Yu, H.; Kubo, A.; Matsuo, Y.; Misawa, H. Direct Imaging of the Near Field and Dynamics of Surface Plasmon Resonance on Gold Nanostructures Using Photoemission Electron Microscopy. *Light: Sci. Appl.* **2013**, *2*, No. e118.
(77) Podbiel, D.; Kahl, P.; Makris, A.; Frank, B.; Sindermann, S.; Davis, T. J.; Giessen, H.; Horn-von Hoegen, M.; Meyer zu Heringdorf, F.-J. Imaging the Nonlinear Plasmoemission Dynamics of Electrons from Strong Plasmonic Fields. *Nano Lett.* **2017**, *17*, 6569−6574.